Sparse denoising and adaptive estimation enhances the resolution and contrast of fluorescence emission difference microscopy based on array detector

Sylvain Prigent, Stéphanie Dutertre, Aurélien Bidaud-Meynard, Giulia Bertolin, Grégoire Michaux, Charles Kervrann

Sparse denoising and adaptive estimation enhances the resolution and contrast of fluorescence emission difference microscopy based on array detector

Sylvain Prigent[1,2], Stéphanie Dutertre[3], Aurélien Bidaud-Meynard[4], Giulia Bertolin[4], Grégoire Michaux[4], and Charles Kervrann[1,2]

[1] *SERPICO Project-Team, Inria-Rennes Bretagne Atlantique, F-35042 Rennes Cedex, France*
[2] *UMR 144, CNRS, Institut Curie, PSL Research University, Sorbonne Universités, F-75005 Paris, France*
[3] *Univ Rennes, UMS Biosit, MRic, F-35000 Rennes, France*
[4] *Univ Rennes, CNRS, IGDR (Institute of Genetics and Development of Rennes), UMR 6290, F-35000 Rennes, France*
[*] *Corresponding author: charles.kervrann@inria.fr*

Array detector allows a resolution gain for confocal microscopy by combining images sensed by a set of photomultipliers tubes (or sub-detectors). Several methods have been proposed to reconstruct a high-resolution image by linearly combining sub-detector images, especially the fluorescence emission difference (FED) technique. To improve the resolution and contrast of FED microscopy based on array detector, we propose to associate sparse denoising with spatial adaptive estimation. We show on both calibration slides and real data that our approach applied to the full stack of spatially reassigned detector signals, enables to achieve a higher reconstruction performance in terms of resolution, image contrast, and noise reduction.

The principle of array detector confocal microscopy is to replace the point detector by a set of $N_D = 32$ sub-detectors circularly arranged around a central detector [1] (see Fig. 1). Each sub-detector has a diameter of 0.2 AU (Airy Unit). The first inner ring grouping the $N = 7$ central detectors has a diameter of 0.6 AU, the second inner ring grouping the $N = 19$ detectors has a diameter of 1 AU, and the full detector has a diameter of 1.25 AU. If $N = 7, 19$ and 32, the resulting images are equivalent to pseudo-confocal images with a pinhole at 0.6 AU, 1 AU, and 1.25 AU, respectively. With this array detector approach, the optical resolution is no longer determined by the size of a single pinhole but depends on the relative positioning of sub-detectors, each acting as a small pinhole and capturing a slightly different view on the sample. Also, more light is collected and the reconstructed image has a higher signal-to-noise ratio (SNR). Nevertheless the estimation of the high-resolution image from sub-detectors is not straightforward. Since the emergence of this technology, two categories of methods have been investigated for image reconstruction: i) the methods based on the linear combination of sub-detectors [2–6] allow either a gain of contrast or a gain of resolution but not both; ii) the deconvolution-based methods allow both contrast and resolution gain, but may create artifacts, especially if the point spread function (PSF) of the set-up is not well calibrated.

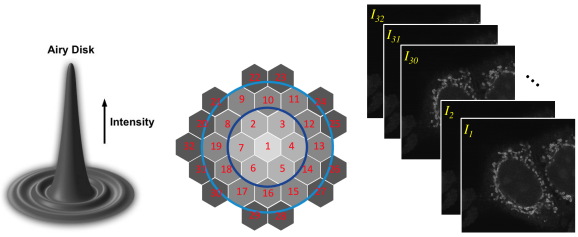

Fig. 1. Scheme of the array detector and image stack. The $N_D = 32$ sub-detectors are hexagonal and arranged around the central sub-detector. The dark blue (resp. light blue) circle highlights the group of $N = 7$ (resp. $N = 19$) central detectors.

In this Letter, we propose an original approach which associates sparse denoising with spatial adaptive estimation to estimate a high-quality fluorescence emission difference (FED) image from the stack of low/high frequency images of array detector. Conventional FED microscopy scans twice the sample, first with a point shape illumination, and second with a donut shape illumination; the FED image is then defined as the difference between these two images. FED based on array detector is similarly obtained by subtracting the "outer" ring of sub-detectors to the "inner" sub-detectors (see Fig. 1). Here, we focus on the IFED [4, 5] and ISFED [6]) techniques since they are considered as the best performant linear methods in terms of spatial resolution. Unfortunately, the IFED and ISFED images are generally very noisy. To overcome this difficulty, we propose to improve the signal-to-noise ratio and the contrast of the IFED and ISFED images by assuming that the true high-resolution image is smooth and sparse. Unlike traditional techniques, our approach is not based on deconvolution, and therefore no PSF calibration which may be tricky with array detector; in the ideal case, the PSF should be estimated separately for each detector.

Based on the IFED [4, 5] and ISFED [6] techniques, our approach amounts to estimating a high-resolution image f as follows:

$$f(x) = u(x) - \epsilon(x)v(x), \quad \textbf{(1)}$$

where $f(x)$ is the fluorescence intensity estimated at the spatial position $x \in \Omega$ (Ω denotes the image domain), and $\epsilon(x) > 0$ is a spatially-varying subtraction factor. Inspired from IFED [4, 5], the images u and v are defined as:

$$\text{IFED-SDen} \begin{cases} u &= \arg\min_u \frac{1}{2}\sum_{i=2}^{N} \|u - I_i\|_2^2 + \lambda R_\rho(u), \\ v &= \arg\min_v \frac{1}{2}\sum_{i=N+1}^{N_D} \|v - I_i\|_2^2 + \lambda R_\rho(v), \end{cases} \quad \textbf{(2)}$$

where $I_i(x)$ (see Fig. 1 (right)) denotes the fluorescence intensity observed at position x sensed by the sub-detector with index i, $N \in \{7, 19\}$, and $R_\rho(\cdot)$ is a sparse-promoting regularization term defined as [7]:

$$R_\rho(w) = \sum_{x\in\Omega} \sqrt{\rho^2 \|\mathcal{H}w(x)\|_F^2 + (1-\rho)^2 w(x)^2}, \quad \textbf{(3)}$$

where w denotes either u or v. Unlike conventional IFED, I_1 is not used in (2); it will serve further to estimate $\epsilon(x)$ at each spatial position and to estimate the sparse denoised IFED (IFED-SDen) image following (1). In (3), $\|\cdot\|_2$ and $\|\cdot\|_F$ denotes the Euclidean norm and Frobenius norm, respectively, and λ is a regularization parameter that controls the amount of smoothing and depends on the level of noise in the raw images. Finally, $\rho \in [0, 1]$ is a weighting parameter that balances the Hessian term $\|\mathcal{H}w(x)\|_F^2$ used to encourage smooth variations of the signal and the intensity term w that "weakly", "moderately" or "strongly" encourages sparsity in the restored image (see details in [7]).

Similarly, inspired from ISFED [6], the images u and v are defined as:

$$\text{ISFED-SDen} \begin{cases} u &= \arg\min_u \frac{1}{2}\sum_{i=2}^{N_D} \|u - \tilde{I}_i\|_2^2 + \lambda R_\rho(u), \\ v &= \arg\min_v \frac{1}{2}\sum_{i=2}^{N_D} \|v - I_i\|_2^2 + \lambda R_\rho(v), \end{cases} \quad \textbf{(4)}$$

where $\tilde{I}_i(x)$ is the intensity at pixel x sensed by the sub-detector i, spatially co-registered to the central detector $i = 1$ (Fig. 1), and $R_\rho(\cdot)$ is the sparse-promoting regularization term given in (3). Unlike conventional ISFED, I_1 and $\tilde{I}_1$ are not used in (2); they will serve to estimate $\epsilon(x)$ at each spatial position, and further, to compute the sparse denoised ISFED (ISFED-SDen) image following (1). Note that if u and v are defined as the sum of the N_D co-registered sub-detectors and the sum of the N_D sub-detectors, respectively, and $\epsilon(x) = \epsilon$ is constant, f in (1) is nothing else than the ISFED image [6], u is the image scanning image (ISM) [2, 3], and v is a pseudo-confocal image with a pinhole of 1.25 AU. Unlike basic sums of sub-detectors, our sparse denoiser (named SPITFIR(e) [7]) which amounts to minimizing global energies given in equations (2) and (4), is robust to Poisson-Gaussian noise and is able to both enhance signals and to estimate a uniform and dark background in 2D-3D confocal microscopy images.

Our content-aware approach may be then considered as a more general technique than IFED or ISFED, which is also improved by adaptively estimating a subtractor factor ϵ at each spatial position (see (1)). The performance of the ISFED and IFED methods actually depends on the calibration of the ϵ subtraction factor assumed to be constant. In [5], the authors showed that by setting $\epsilon = 0.3$ yielded very satisfying experimental results. Nevertheless, we experimentally observed that ϵ should be adaptively adjusted according to SNR; for low SNR values $\epsilon = 0.3$ is appropriate, but ϵ must be increased to 1.0 to accommodate high SNR values. These results suggested the development of a data-driven method to automatically set ϵ as investigated in [8]. First, we assume that the (central) image $I_1 = h * f + \eta$ is a degraded version of the IFED [4, 5] or ISFED [6] image, where η is a Gaussian noise with spatially-varying variance $\sigma^2(x)$, h denotes the 2D spatial response of the device that represents the blur related to the optical system (or PSF) assumed to be linear shift-invariant, and $*$ denotes the convolution operator. Here, the assumption of a spatially homogeneous Gaussian noise does not hold as u and v have been estimated by our sparse denoiser. To locally determine ϵ, let us consider a spatial neighborhood $\Omega(x)$ centered at position x and denote $n = |\Omega(x)|$ the number of pixels in $\Omega(x)$. The size of $\Omega(x)$ is fixed for all spatial positions (e.g., $|\Omega(x)| = 5 \times 5$ pixels) and $\epsilon(x)$ is assumed to be constant in $\Omega(x)$. Define the local Stein's unbiased risk estimate (SURE) that it is an unbiased estimate of the mean-squared error of $f(x)$ at position $x \in \Omega$ as:

$$SURE(x) = (2\text{div}_{I_1}(f)(x) - n)\sigma^2(x) + \sum_{y\in\Omega(x)} (I_1(y) - (h*f)(y))^2, \quad \textbf{(5)}$$

where $\text{div}(\cdot)$ denotes the divergence of f wrt I_1. Unlike [8], as I_1 is not included in (2) and (4), $\text{div}_{I_1}(f)(x) = 0$. Therefore, solving $\frac{\partial SURE(x)}{\partial \epsilon(x)} = 0$ gives the closed-form solution:

$$\epsilon(x) = -\frac{\sum_{y\in\Omega(x)} (I(y) - (h*u)(y))(h*v)(y)}{\sum_{y\in\Omega(x)} (h*v)^2(y)}, \; x \in \Omega. \quad \textbf{(6)}$$

The resulting subtraction factor map ϵ (see illustrations in Supplementary Figs. S3-S5) is used in (1) to reconstruct high-resolution images. In what follows, h in (6) is assumed to be Gaussian. Unlike deconvolution, the choice of the PSF size is not critical; it is set to 1.2 by default in all our experiments. Meanwhile, the parameters of SPITFIR(e) are calibrated from the noisy images and require no manual adjustment as explained in [7].

In our experiments, our baseline method is the image scanning microscopy (ISM) technique as it generally produces higher resolved images than pseudo-confocal images. We compared our approach (IFED-SDen (1)-(2), ISFED-SDen (1)-(4)) to conventional IFED, ISFED, and ISM techniques, as well as to three additional reconstruction methods based on deconvolution (see Table 1): ISM-W (Wiener), ISM-SDeconv, AD-SDeconv. The two latter ones correspond to the deconvolution with SPITFIR(e) [7] of the ISM image and of the native array data, respectively:

$$f_{ISM-SDeconv} = \arg\min_f \frac{1}{2}\|Hf - I_{ISM}\|_2^2 + \lambda R_\rho(f), \quad \textbf{(7)}$$

ISM [2, 3]	: Image Scanning Microscopy
IFED [4, 5]	: Image Fluorescence Emission Difference
ISFED [6]	: Image Scanning Fluorescence Emission Difference
ISM-W	: Wiener deconvolution of ISM image
ISM-SDeconv (7)	: Sparse deconvolution of ISM image
AD-SDeconv (8)	: Sparse deconvolution of array detector
IFED-SDen (1)-(2)	: Sparse denoising of IFED image
ISFED-SDen (1)-(4)	: Sparse denoising of ISFED image

Table 1. List of methods for high-resolution image estimation.

$$f_{AD-SDeconv} = \arg\min_f \frac{1}{2}\sum_{i=1}^{N_D} \|Hf - I_i\|_2^2 + \lambda R_\rho(f), \quad (8)$$

where H represents the point spread function (PSF) (matrix form). In (8), AD-SDeconv performs both the merging of multiple images $\{I_1, \cdots, I_{N_D}\}$ and sparse deconvolution at once. The size of the PSF in (7) and (8), selected in the range $[1.0; 2.0]$, is set to 1.5 pixel by default as it provided the most satisfying results.

First, we considered an image depicting a ring shape object taken from the Argolight calibration slide, whose surface is known to be spatially smooth. The "donut" pattern (only one "donut" is depicted in Figure 2(a)) consists of a matrix of rings, separated by 15 μm (see Supplementary Fig. S1). The typical transverse diameter (in the XY plane) of each ring is about (0.7 ± 0.1) μm. Figure 2(a) shows the high-resolution images obtained with each method. First, we can notice that the ISM image has a high contrast but a low resolution. The IFED and ISFED images have low SNRs due to sub-detector subtraction, but a higher resolution than the ISM image. At first glance, the two deconvolution methods ISM-W and ISM-SDeconv produced higher resolution images. The AD-SDeconv algorithm produced an image where the ring that appears to be visually thinner and more homogeneous than the ISM-W and ISM-SDeconv images. Finally, the IFED-SDen and ISFED-SDen images have higher SNRs than the IFED and ISFED images and the resolutions are improved, as confirmed below. In each case, we computed the average profiles from 12 intensity profiles (shown in Supplementary Fig. S2) along straight lines traced across the "donut" and inclined by 15 degrees for each other as displayed in (b; left). In Fig. 2(b; right), we only plotted the average profiles of the ISM, ISFED, AD-SDen, and ISFED-SDen methods for the sake of visualization. The average profiles of the eight methods are plotted in Supplementary Fig. S2(b). From the conventional full width at half maximum (FWHM) criteria, the average thickness of the donut is 313 nm with the baseline ISM method. The individual profiles obtained with IFED and ISFED methods appear to be very noisy as shown in Supplementary Fig. S2); the average thickness of the donut is 275 nm and 264 nm for IFED and ISFED, respectively. The deconvolution methods that take the ISM image as input produced high-resolution images with thinner and smoother peaks. The resulting average thickness are 260 nm (ISM-W) and 244 nm (ISM-SDconv). The AD-SDconv algorithm provided the best deconvolution results; the profiles are less noisy, thinner (average thickness: 232 nm) and show a slightly lower variance around the donut than those produced by the two other deconvolution methods. The resolution of IFED-SDen image is higher than ISM-W but is still inferior to the resolution achieved with the other deconvolution techniques. Finally, the best overall result was obtained with ISFED-SDen as the estimated resolution is 209 nm, which is significantly higher than those obtained with the other methods. The ISFED-SDen image contains small details that were actually removed with the deconvolution methods, including AD-SDeconv.

Second, we applied the competing methods to an image depicting vertical line pattern from the Argolight calibration slide. This pattern contains ten groups composed of two pairs of vertical lines for which the distance between two pairs of lines decreases from 550 nm to 100 nm with 50 nm steps (see description in Fig. 3(a)). To estimate the spatial resolution, we measured the contrast C (intensity gap) as follows: $C = (I_{max} - I_{min})/(I_{max} - I_{background})$, where I_{max} is the maximum intensity value measured on vertical lines, I_{min} is the mini-rated, the contrast C increases up to a maximum of 1 as

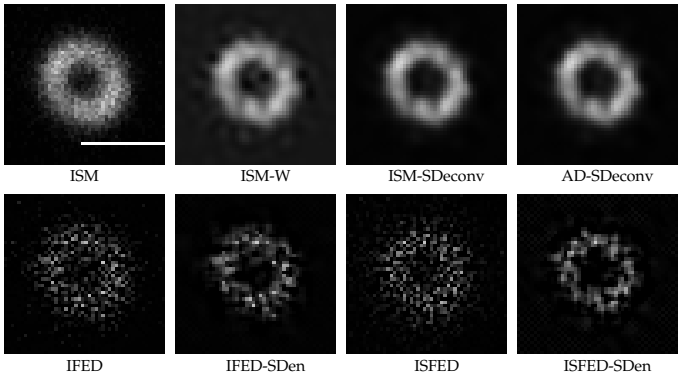

(a) High-resolution images estimated with the eight methods.

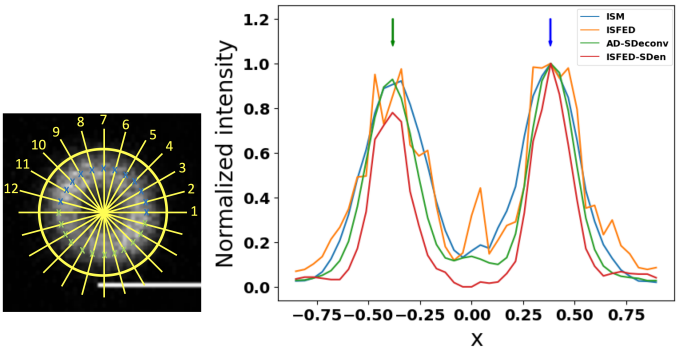

(b) Average profiles obtained with ISM, ISFED, AD-SDeconv, and ISFED-SDen.

Fig. 2. High-resolution reconstruction obtained with the eight methods applied to the "donut" image from the Argolight calibration slide (ZEISS Airyscan microscope). (a) high-resolution images. All the images were normalized in the range [0, 1]. Scale bar: 1.0 μm. (b) Average profiles of ISM, ISFED, AD-SDeconv, and ISFED-SDen (right) computed from 12 registered intensity profiles along straight lines traced across the "donut and inclined by 15 degrees for each other (left). The green and blue crosses (left) and arrows (right) indicate the first and second peaks. The X axis represents the distance in microns to the "donut" center computed from the registered profiles.

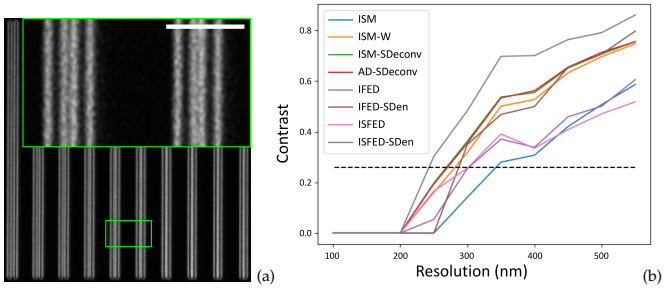

Fig. 3. Resolution measurement using the line pattern. (a) image of the pattern (scale bar: 3.0 μm). The image is normalized in the range $[0; 1]$. The distance between lines decreases from 550 nm to 100 nm with 50 nm steps. (b) Contrasts $C \in [0, 1]$ for each method applied to the 10 line patterns. The black dashed line shows the arbitrarily chosen resolution threshold: ISM: 344 nm; IFED: 304 nm; ISFED: 303 nm; IFED-SDen: 297 nm; ISM-W: 283 nm; AD-SDeconv: 272 nm; ISM-SDeconv: 270nm; ISFED-SDen: 260 nm.

mal intensity value measured between two pairs of vertical lines, and $I_{background}$ is the intensity value computed over a region of interest in the image background. If the two pairs of lines are very close and slightly overlap, the contrast C is close to 0 as $I_{max} \approx I_{min}$. On the contrary, if two pairs of lines are well sepa-

$I_{min} \approx I_{background}$. To improve robustness to noise, the I_{max} and I_{min} values are averaged values, computed from the sum of intensities along the vertical lines (i.e, projection along the Y axis). With this Argolight sample, it turns out that a contrast below 26.5% (see Argolight documentation) means that objects at the line resolution cannot be distinguished. The measured contrasts are plotted in Fig. 3(b). As in Fig. 2, we can clearly notice the ISFED-SDen curve is above all other curves, suggesting that the best resolutions are obtained with ISFED-SDen first, and AD-SDeconv and ISM-SDeconv, second. The ϵ map is shown in Supplementary Fig. S3.

To evaluate the performance on real data, we first applied the eight reconstruction algorithms to an image depicting mitochondria in MCF7 cells expressing mito-GFP. In Fig. 4(a), we display the best results (in terms of resolution) obtained with the ISFED, ISFED-SDen, and AD-SDeconv methods. As before, the SNR is lower with the ISFED method when compared to AD-SDeconv. Finally, ISFED-SDen achieved a resolution higher than ISFED, while significantly reducing noise. If we compare the intensity profiles along the yellow straight lines drawn in Fig. 4(a) and estimated by the ISM, ISFED, AD-SDen, and ISFED-SDen methods (see Fig. 4(c); left), we can notice that ISFED-SDen produced the thinner profiles, which are smoother than the ISFED profiles. The comparison with the eight methods is shown in Supplementary Figs. S6(a) and S7(a).

Furthermore, we applied the reconstruction methods to an image depicting intestinal microvilli from a young adult C. elegans worm *in vivo* expressing the ERM-1::mNeonGreen fusion protein (ERM-1 is specifically localized in intestinal microvilli [9, 10]) (see Fig. 4(b)). The ISFED, AD-SDeconv, and ISFED-SDen better enhance the 100 nm large microvilli. On this particular example depicting a pattern with high spatial frequencies, one can notice horizontal-line artifacts in the ISFED images, induced by the the scanning process and imperfect registration of sensors. In Fig. 4(c; right), the cross-section profiles along the straight yellow lines drawn in Fig. 4(b) suggest that ISFED-SDen better reveals the structure, removes background, and significantly reduces the horizontal-line artifacts in the ISFED image (see Fig. 4(b)). The comparison of intensities profiles estimated with all methods is shown in Supplementary Figs. S6(b) and S7(b). The ϵ maps used to compute the ISFED-SDen images in Fig. 4 are shown in Supplementary Figs. S4 and S5.

In this Letter, we proposed a high-resolution reconstruction method applied array detector that combines sparse denoising and spatial adaptive estimation, and automatically adapts to the level of noise observed in the raw images. Our ISFED-SDen approach does not require PSF calibration required to analyze real datasets and outperforms deconvolution techniques. The estimation of parameters is data-driven or set to default values once for all (e.g., $|\Omega(x)| = 5 \times 5$ pixels and the Gaussian PSF size (6) is set to 1.2 pixel). About 30 seconds of computing time (core i7 CPU) is required to estimate a 512×512 image with the ISFED-SDen and IFED-SDen methods.

Software availability. The software can process 2D and 3D images. A python library can be found here: https://github.com/sylvainprigent/sairyscan. A napari plugin can be dowloaded here: https://github.com/sylvainprigent/napari-sairyscan.

Funding. France-BioImaging ANR-10-INBS-04-07.

Disclosures. The authors declare no conflict of interest.

Supplemental document. See Supplement 1 for supporting content.

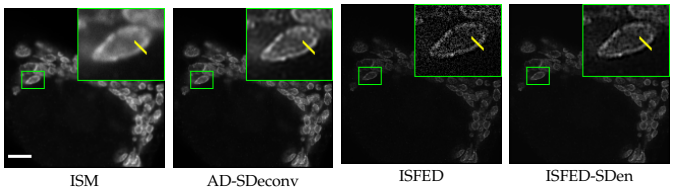

(a) MCF7 cells expressing mito-GFP. Scale bar: 1 μm.

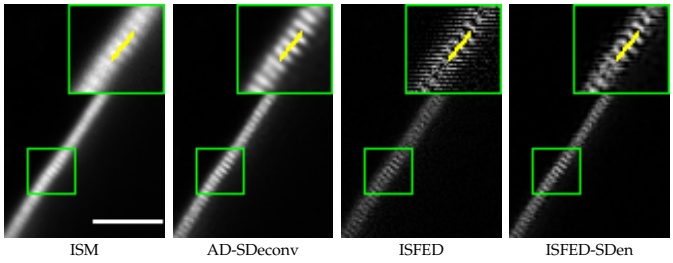

(b) C. elegans sample (ERM-1::mNeonGreen fusion protein). Scale bar: 2 μm.

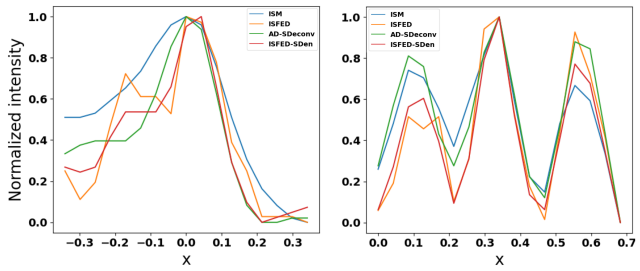

(c) Intensity profiles for MCF7 cells (left) and C. elegans sample (right).

Fig. 4. Images obtained with the eight methods and normalized in the range $[0; 1]$. High resolution images depicting MCF7 cells (a) and C.elegans sample (b), respectively. (c) The intensity profiles along the straight yellow lines displayed in (a) and (b) are estimated by the ISM, ISFED, AD-SDen, and ISFED-SDen methods. The X axes are graduated as the distances to the line centers (in microns).

Data availability. Data acquisition was performed at the MRic Microscopy Rennes Imaging Center (France) with a confocal (Zeiss LSM 880) with airyscan microscope. The argoslide is the Argo-Z slide SLG-121 (Argolight S.A.). Objective used is the Plan-Apochromat 63x/1.4 Oil DIC M27. For excitation of the slide, the 488 laser beam was used with a BP 495-550 + LP 570 emission filter set. ERM-1 (aka ezrin in mammals) is an actin crosslinker enriched in the microvilli that has been endogenously tagged with Neongreen fluorophore by CRISPR-Cas9 [9]. The microvilli patterns in worms, as well as the localization of ERM-1 in these structures, have been characterized in [10]. The results presented in this Letter may be obtained from the authors upon reasonable request.

REFERENCES

1. K. Weisshart, ZEISS Technol. Note (2014).
2. C. B. Müller and J. Enderlein, Phys. Rev. Lett. **104**, 198101 (2010).
3. C. J. R. Sheppard, S. B. Mehta, and R. Heintzmann, Opt. Lett. **38**, 2889 (2013).
4. Y. Ma, C. Kuang, Y. Fang, B. Ge, D. Li, and X. Liu, Opt. Lett. **40**, 4627 (2015).
5. B. Ge, Y. Wang, Y. Huang, C. Kuang, Y. Fang, P. Xiu, Z. Rong, and X. Liu, Opt. Lett. **41**, 2013 (2016).
6. Y. Li, S. Liu, D. Liu, S. Sun, C. Kuang, Z. Ding, and X. Liu, J. Microsc. **266** (2017).
7. S. Prigent, H. Nguyen, L. Leconte, C. Valades-Cruz, B. Hajj, J. Salamero, and C. Kervrann, Sci Reports 10.1038/s41598-022-26178-ys (2023).
8. S. Prigent, S. Dutertre, and C. Kervrann, In Proc. IEEE Int. Conf. Acoust. Speech Signal Process. (ICASSP) pp. 1075–1079 (2020).
9. A. Bidaud-Meynard, O. Nicolle, M. Heck, Y. Le Cunff, and G. Michaux, Development **146** (2019).
10. A. Bidaud-Meynard, F. Demouchy, O. Nicolle, A. Pacquelet, S. Kumar Suman, C.N. Plancke, F.B. Robin, and G. Michaux, Development **148** (2021).

Sparse denoising and adaptive estimation enhances the resolution and contrast of fluorescence emission difference microscopy based on array detector

SUPPLEMENTAL DOCUMENT

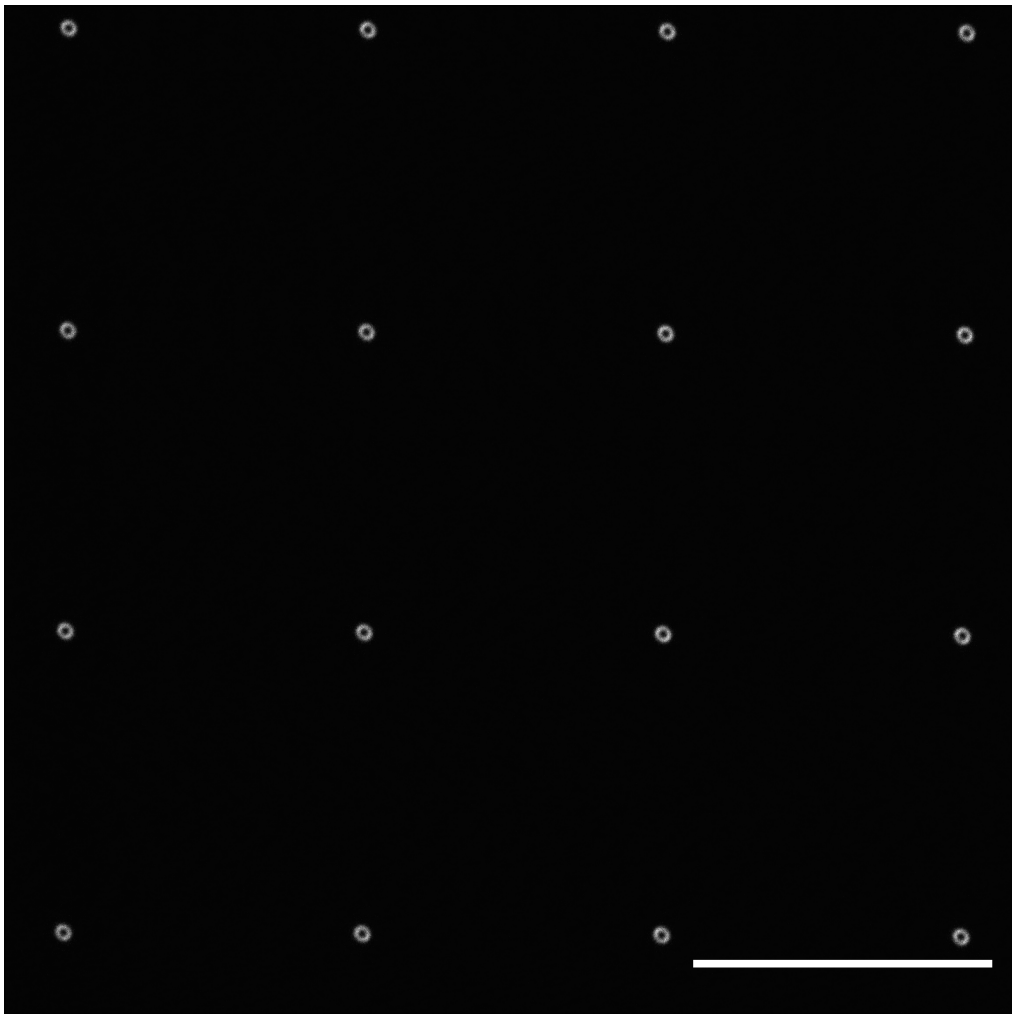

Fig. S1. Image depicting the "donut" pattern taken from the Argolight calibration slide. The "donut" pattern consists of a matrix of rings, separated by 15 μm. The typical transverse diameter (in the XY plane) of each "donut"" is about (0.7 ± 0.1) μm. Scale bar: 15.0 μm.

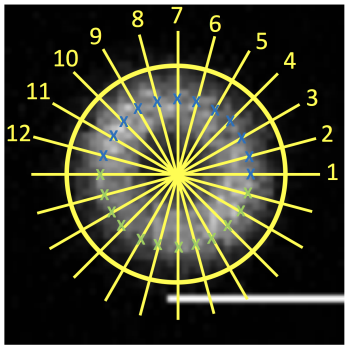

(a) Twelve inclined straight lines across the "donut".

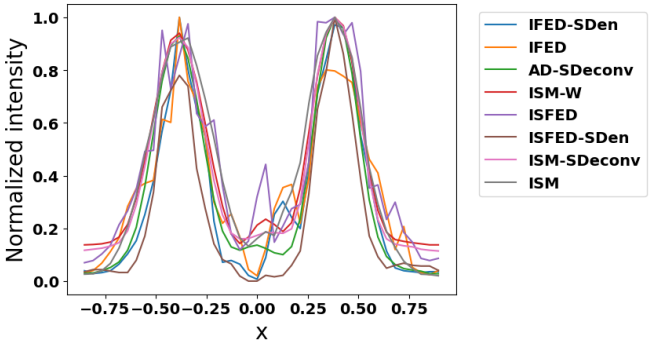

(b) Average profiles obtained with the eight methods.

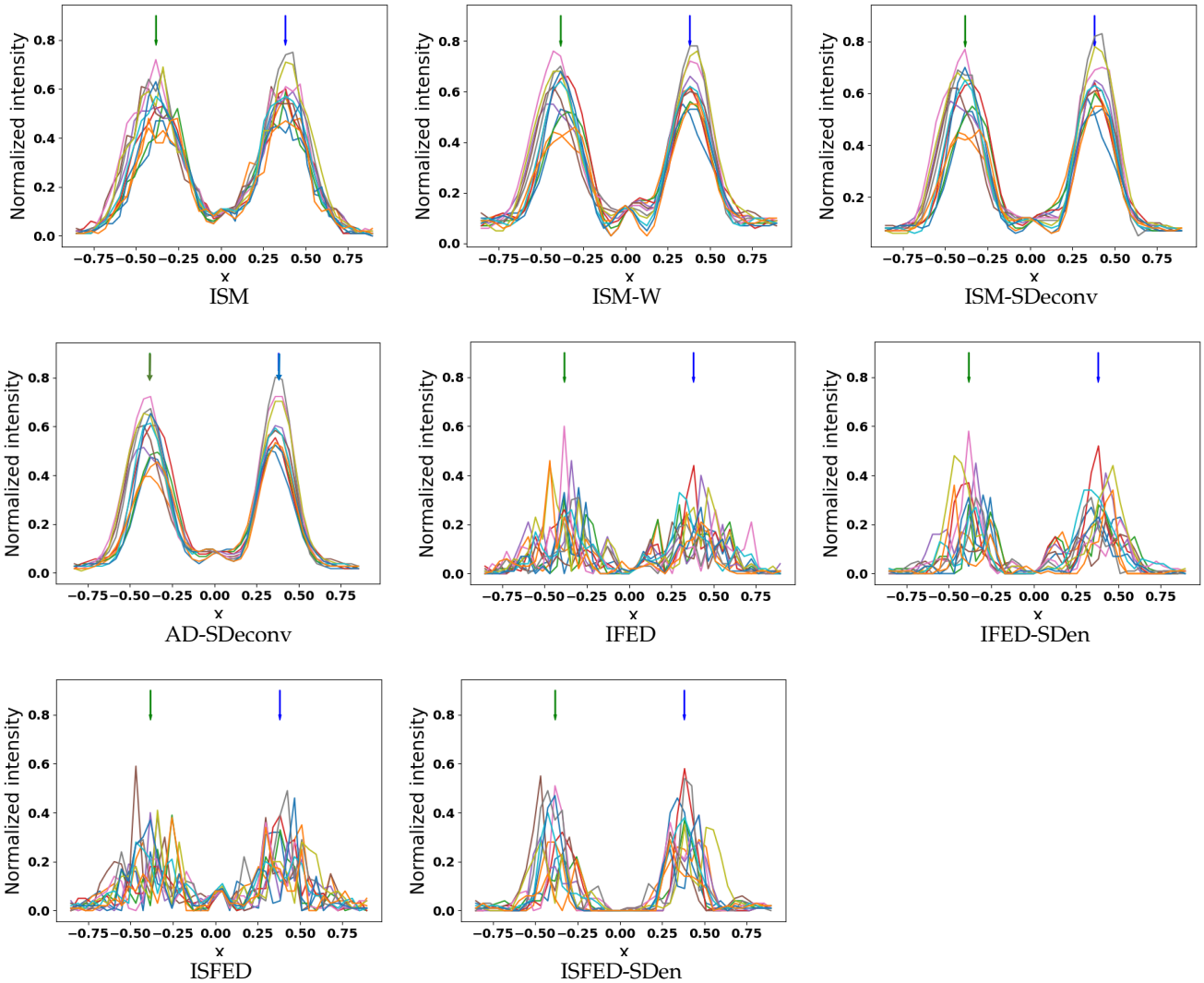

(c) Intensity profiles across the "donut" (one different color for each angle).

Fig. S2. Intensity profiles obtained with the eight methods applied to the "donut" image from the Argolight calibration slide (ZEISS Airyscan microscope). Plots of the averages profiles for each method (b) computed from 12 intensity profiles (shown in (c)) along straight lines traced across the "donut" and inclined by 15 degrees for each other as displayed in (a). The X axis represents the distance in microns to the "donut" center estimated from the registered profiles.

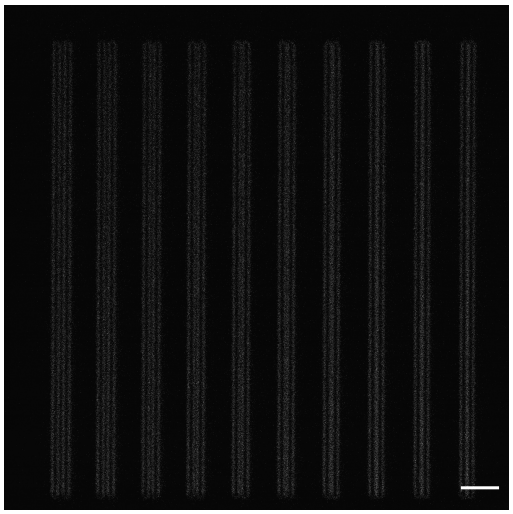

(a) I_1

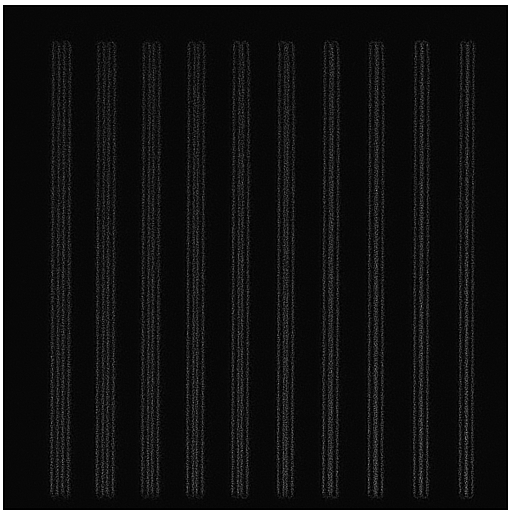

(b) ISFED-SDen

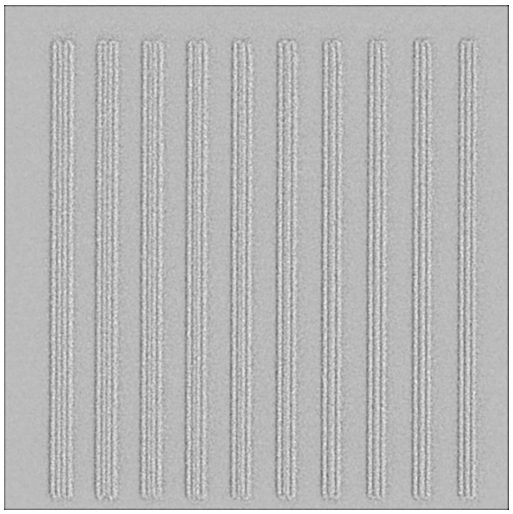

(c) ϵ map

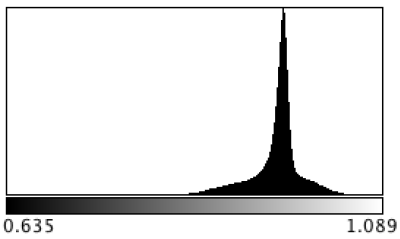

(d) Histogram of ϵ map

Fig. S3. Estimation of ϵ map computed from the array detector (Argolight calibration slide). (a) Image I_1 (scale bar: 3.0 μm); (b) Sparse denoised IFSED image. (c) ϵ map. (d) Histogram of the ϵ map (mean: 0.645; mode: 0.969).

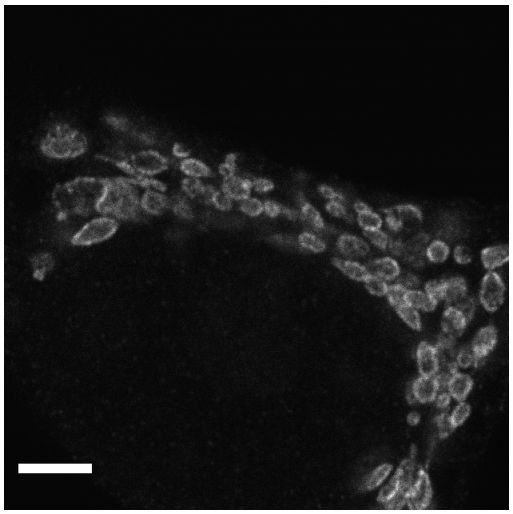

(a) I_1

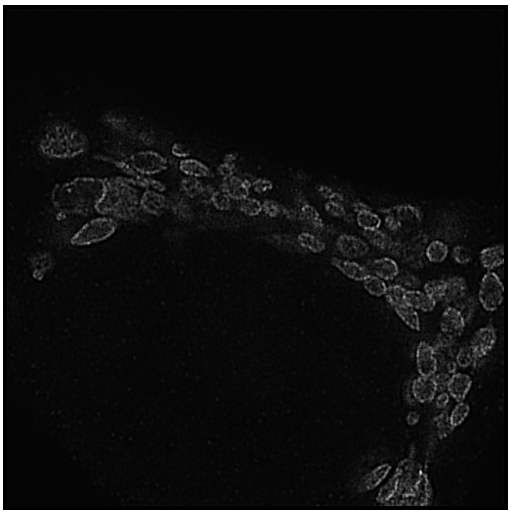

(b) ISFED-SDen

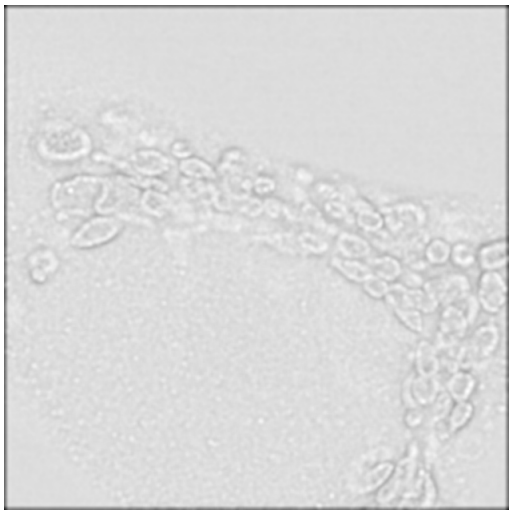

(c) ϵ map

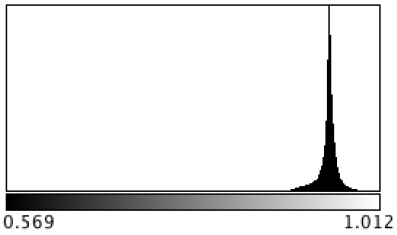

(d) Histogram of ϵ map

Fig. S4. Estimation of ϵ map computed from the array detector (MCF7 cells expressing mito-GFP). (a) Image I_1 (scale bar: 1.0 μm); (b) Sparse denoised IFSED image. (c) ϵ map. (d) Histogram of the ϵ map (mean: 0.948; mode: 0.953).

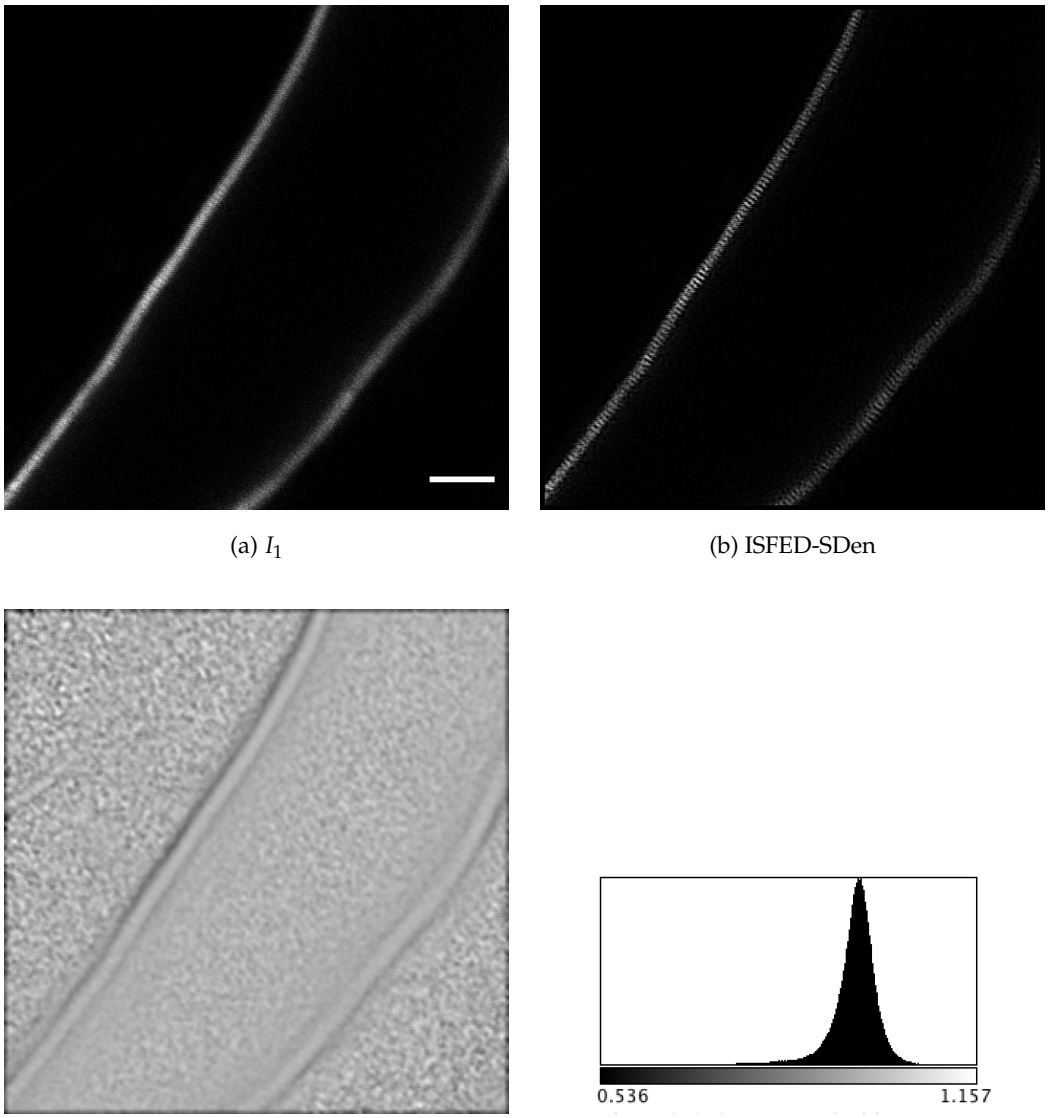

(a) I_1 (b) ISFED-SDen

(c) ϵ map (d) Histogram of ϵ map

Fig. S5. Estimation of ϵ map computed from the array detector (C. elegans sample expressing the ERM-1::mNeonGreen fusion protein). (a) Image I_1 (scale bar: 2.0 μm); (b) Sparse denoised IFSED image. (c) ϵ map. (d) Histogram of the ϵ map (mean: 0.955; mode: 0.966).

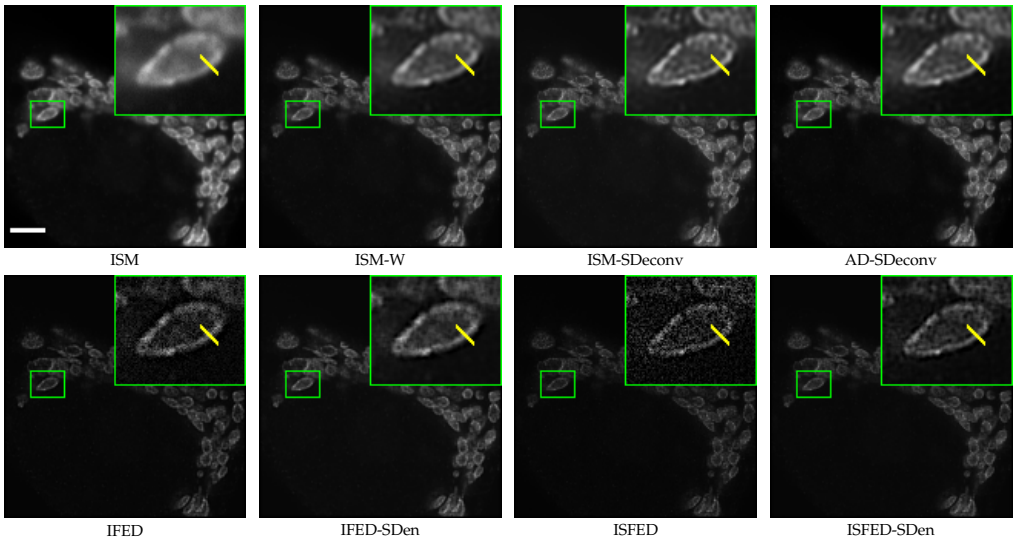

(a) MCF7 cells expressing mito-GFP. Scale bar: 1 μm.

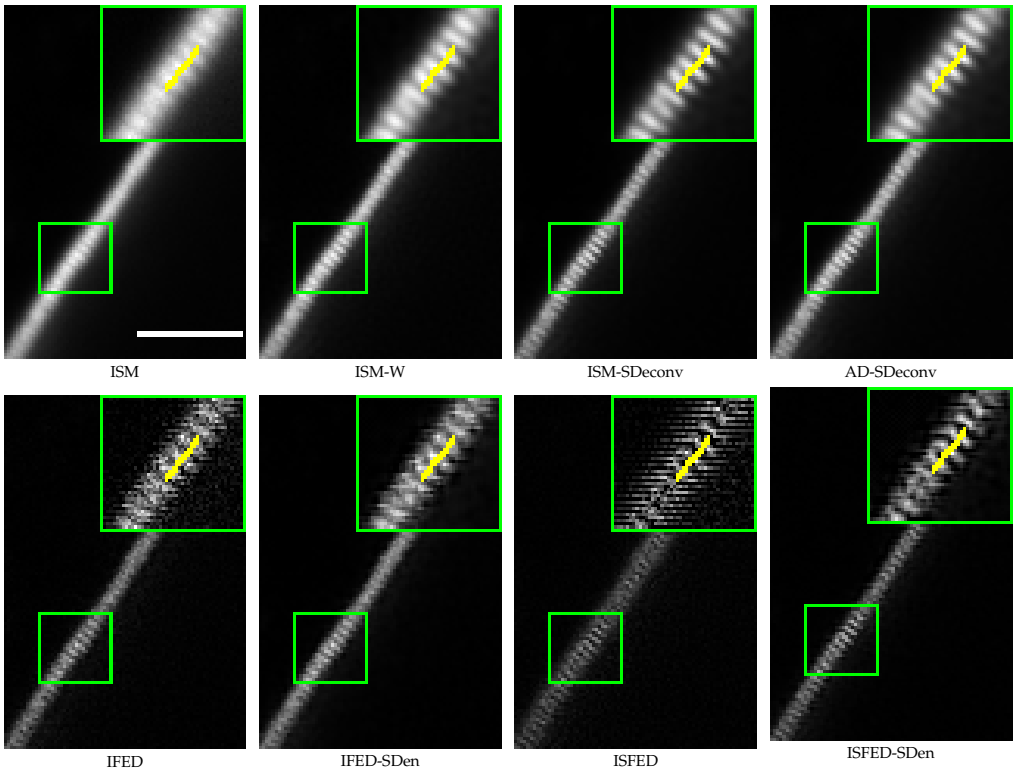

(b) C. elegans sample (ERM-1::mNeonGreen fusion protein). Scale bar: 2 μm.

Fig. S6. Images obtained with the eight methods and normalized in the range $[0; 1]$. (a) High resolution images depicting MCF7 cells expressing mito-GFP (labelling mitochondria). (b) High resolution images depicting C.elegans sample expressing the ERM-1::mNeonGreen fusion protein.

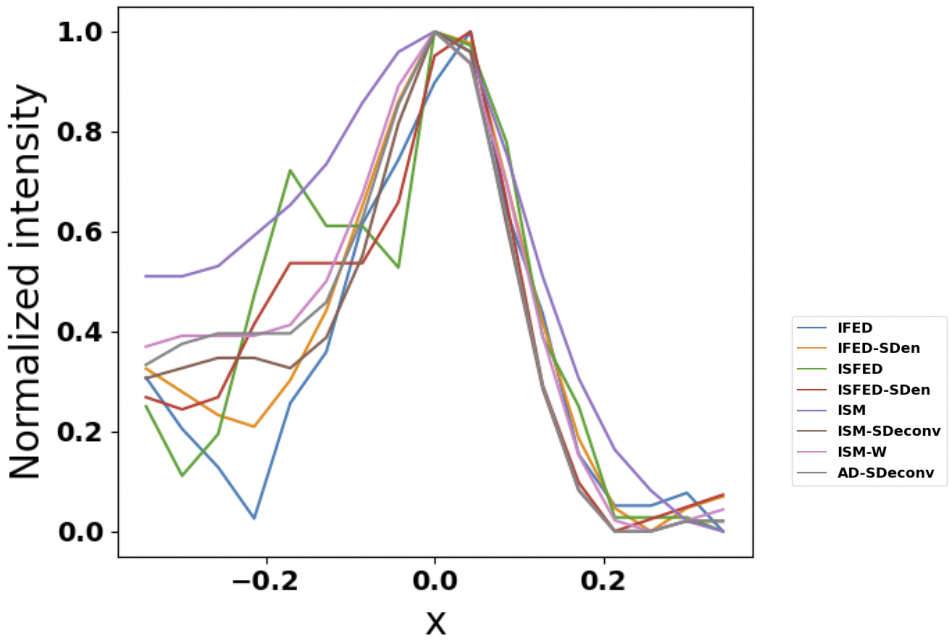

(a) MCF7 cells.

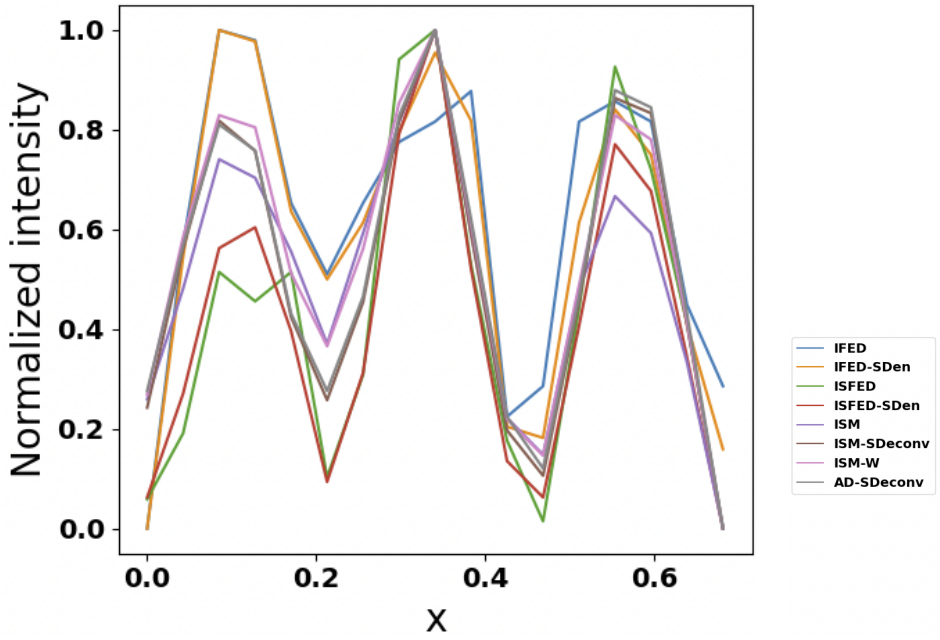

(b) C. elegans sample.

Fig. S7. Profiles obtained with the eight methods applied to the images depicting MCF7 cells (a) expressing mito-GFP (labelling mitochondria) and C.elegans sample (b) expressing the ERM-1::mNeonGreen fusion protein, respectively (see Supplementary Fig. S6). The intensity profiles are estimated along the straight yellow lines displayed in Supplementary Fig. S6(a) and Fig. S6(b), respectively. The X axes are graduated as the distances to the line centers (in microns).